Advanced Composites and Hybrid Materials (2025) 8:133
https://doi.org/10.1007/s42114-025-01234-z

RESEARCH

Bifunctional mixed-valence ruthenium heterostructure for robust electrocatalytic water splitting in acid media

Xinyu Xie[1,2] · Yixiao Zhang[2] · Yang Qin[2] · Jianbo Wu[1] · Ming Lei[3] · Kai Huang[2] · Ruyue Wang[2] · Peng Du[1]

Received: 16 October 2024 / Revised: 18 December 2024 / Accepted: 9 January 2025
© The Author(s) 2025

Abstract

The incorporation of non-metal dopants can significantly enhance catalytic activity and improve stability. Furthermore, the creation of heterostructures is particularly advantageous to facilitate charge transfer and optimize electronic properties. This study presents an effective bifunctional mixed-valence Ruthenium heterostructure synthesized through a cascading process involving grinding with carbon nitride and subsequent thermal treatment. The catalyst exhibits outstanding electrocatalytic performance with remarkably low overpotentials of 197 mV for the oxygen evolution reaction (OER) and 24.8 mV for the hydrogen evolution reaction (HER), respectively, with the stability exceeding 24 h at a current density of 10 mA cm^{-2} in acidic media. Additionally, when employed in an acidic oxygen water splitting (OWS) electrolyzer, the bifunctional catalyst demonstrates excellent activity, achieving an ultralow cell voltage of 1.53 V to sustain 10 mA cm^{-2}. Enhanced performance is attributed to efficient charge transfer and increased exposure of active sites, providing valuable insights for the development of effective acidic water-electrolysis catalysts for sustainable hydrogen production.

Keywords Bifunctional catalyst · Water splitting · Oxygen evolution reaction · Hydrogen production

1 Introduction

In recent years, the utilization of hydrogen as an energy storage medium has attracted substantial academic and industrial interest in recent years, owing to its potential to facilitate sustainable energy systems and decarbonization efforts [1–3]. Among various hydrogen production technologies, water electrolysis powered by renewable energy, particularly proton exchange membrane water electrolysis (PEMWE), is regarded as highly promising due to its high energy efficiency, rapid response capabilities and compatibility with intermittent renewable energy sources [4, 5]. However, the water electrolysis involves kinetically sluggish OER and HER, both requiring continuous changes in intermediate valence states, resulting in overpotentials significantly higher than the theoretical water decomposition voltage [6–8]. This places greater demands on the activity and stability of the catalyst. Therefore, developing highly active, cost-effective, and durable bifunctional electrocatalysts is crucial for optimizing device structure, as it reduces the complexity and cost associated with using separate catalysts, ultimately enhancing the overall efficiency of hydrogen production through water electrolysis [9, 10].

Among all available catalysts in widespread use, noble metal composite catalysts such as platinum (Pt), iridium (Ir) and their oxides have been well-recognized for their superior catalytic activity and selectivity [11–13]. However, the increasing cost of these catalysts is a significant barrier to their practical application. In contrast, ruthenium (Ru) offers a more economical option, and numerous studies have shown that Ru can achieve impressive catalytic performance

Xinyu Xie and Yixiao Zhang are contributed to this work equally.

✉ Peng Du
pengdu@tzc.edu.cn

Kai Huang
huang-kai@bupt.edu.cn

Ruyue Wang
Wangruyue@bise.hrl.ac.cn

[1] Zhejiang Key Laboratory for Island Green Energy and New Materials, School of Materials Science and Engineering, Taizhou University, Taizhou 318000, Zhejiang, China

[2] State Key Laboratory of Information Photonics and Optical Communications, School of Science, Beijing University of Posts and Telecommunications, Beijing 100876, PR China

[3] School of Integrated Circuits, Beijing University of Posts and Telecommunications, Beijing 100876, China

Published online: 18 January 2025

through appropriate structural design and tuning, making it a promising bifunctional catalyst for both OER and HER [14–16]. However, its insufficient durability in acidic media still hinders its practical application [17, 18]. This is mainly arises from the tendency of Ru to undergo valence state changes under high potential conditions, resulting in the formation of unstable high-valence oxides [19–21]. In addition, the participation of lattice oxygen in the reaction generates oxygen vacancies that enhance the catalytic activity for the OER process [22–24]. The rates of water adsorption and surface oxygen migration are insufficient to offset the formation of these vacancies, ultimately leading to cation leaching from the catalyst [25, 26]. Consequently, there is an urgent need to explore effective strategies to optimize the structure of Ru-based oxides and improve their stability.

As research progresses, the design of interfaces and the modulation of electronic structures of composite catalysts have increasingly become critical avenues for improving catalytic performance [27, 28]. By tailoring the interfacial properties of the catalyst, the adsorption capacity of reactants and the activation process of intermediates can be significantly improved. Accordingly, numerous composite-structured catalysts have been designed, demonstrating substantial performance improvements towards various application, such as production of organic chemicals, biofuels and sustainable energy techniques [29–33]. Surface atomic configuration by non-metal doping serves as an effective modification strategy that can enhance the reactivity of catalysts by altering their electronic interactions and surface properties [34, 35]. Non-metallic materials commonly used include C_3N_4, nitrogen-doped carbon materials, sulphur-doped oxides and phosphorus-doped two-dimensional nanosheets [36–38]. However, existing modulation techniques present certain drawbacks, including the introduction of potential defects and nonuniform distribution, which can affect catalytic stability. In addition, the complexity and associated cost of these strategies may inhibit their large-scale application. This makes it imperative to develop more effective and economical strategies to optimize catalyst performance [39]. Recent efforts have focused on the modification of RuO_2 such as transition metal doping, introduction of defects/vacancies and adjustment of surface atomic configurations [40, 41]. An effective approach involves the in-situ formation of heterostructures to design composite catalysts, which significantly optimizes the electronic structure and accelerates interfacial charge transfer efficiency [42, 43]. In addition, the introduction of defects/vacancies can alter the distribution of electronic charges and control disorder within the structure, which plays a crucial role in manipulating the structure of intermediates during electrocatalytic reactions [44, 45].

In this study, a facial strategy was developed to prepare a enhanced catalyst composed of heterostructure of metallic Ru and RuO_x (Ru/RuO_x@CN) through a cascading process combining grinding with C_3N_4 followed by thermal treatment. This optimized catalyst exhibits remarkable bifunctional electrocatalytic performance, with an overpotential of 197 mV for OER and 24.8 mV for HER in acidic media, demonstrating exceptional stability for over 24 h at 10 mA cm^{-2}, surpassing those of commercial Pt/C and RuO_2 catalysts. The enhanced performance of the composite catalyst can be attributed to rapid charge transfer between the heterogeneous structures and the increased exposure of active sites. This strategy offers valuable insights for designing acidic electrolysis catalysts for hydrogen production, especially in improving their activity and st ability.

2 Materials and methods

2.1 Materials

C_3N_4 was purchased from XFNANO Materials Tech Co. Ltd., Ruthenium (IV) oxide (RuO_2, metal-based, 99.9%) and absolute ethanol (C_2H_5OH, 99.8%) were purchased from Aladdin Company. Commercial 20 wt% Pt/C, commercial IrO_2 and Nafion perfluorinated resin solution (5 wt%) were purchased from Sigma-Aldrich. All chemicals were of analytical reagent grade and used as received without further purification.

2.2 Preparation of Ru/RuO_x@CN catalysts

The Ru/RuO_x@CN catalysts were synthesized by a cascading process of grinding and thermal treatment. Typically, powders of 50 mg RuO_2 and 69.1 mg C_3N_4 were directly added into 20 mL of ethanol and sonicated in a high-power sonic bath to obtain a homogeneous suspension. The solution was then transferred to a mortar and ground into a uniform-colored mixture at room temperature. Subsequently, the mixture was thermally treated at 800 °C for 2 h with a heating rate of 10 °C min^{-1} to obtain Ru/RuO_x@CN catalyst under an Ar atmosphere using a rapid heating furnace. The sample was taken out once the furnace temperature was cooled down to room temperature. Various temperatures (700, 750, 800 and 850 °C), treatment durations (0.5, 1 and 2 h), and precursor ratios (RuO_2: C_3N_4 = 1:2, 1:5, 1:10) were employed to prepare comparative samples of different components, with the specific experimental conditions denoted in detail.

2.3 Material characterizations

Scanning electron microscope (SEM) was taken by a scanning transmission electron microscopy (FE-SEM, S-4800, Japan). Transmission electron microscopy (TEM)

observations were performed on a transmission electron microscope (JEM-ARM200F, JEOL, Japan) operated at 200 kV. X-ray diffraction (XRD) patterns were recorded at room temperature using a D/max 2500 V X-ray diffractometer (Rigaku, Japan) attached with Cu Kα radiation of a scanning speed of 8 $^{o}min^{-1}$. XPS analysis was conducted using an X-ray photoelectron spectrometer (Escalab 250 Xi, Thermo Fisher Scientific, MA, USA) with an Al Kα radiation source (1487.6 eV) and a hemispherical analyzer operating at a pass energy of 30.0 eV and an energy step size of 0.05 eV. The C 1 s peak at 284.8 eV served as the internal reference for binding energy calibration. Spectral deconvolution involved Shirley background subtraction and was performed using a Voigt function, combining Gaussian and Lorentzian components.

2.4 Electrochemical characterizations

All electrochemical experiments were performed at room temperature using CHI 760 workstation in a standard three-electrode configuration. A glassy carbon (GC) electrode (diameter: 5 mm; area: 0.196 cm^2) was utilized as the working electrode (WE), while a graphite rod and saturated Ag/AgCl electrode were employed as the counter electrode (CE) and reference electrode (RE), respectively. To prepare the working electrode, 5 mg powders of Ru/RuO_x@CN was dispersed into the mixture solution of ethanol (100 µL) and DI water (800 µL) with 10 wt.% Nafion (100 µL) as the binder to form the catalyst ink and sonicated for 20 min. Then, 40 µL of the catalyst ink was drop-cast onto the surface of the GC electrode and dried in the air. The loading amount of catalyst at working electrode was estimated to be about 0.51 mg cm^{-2}. For comparison, 5 mg of commercial 20% Pt/C, IrO_2 and RuO_2 catalyst inks were also prepared in the same method. All potentials were calibrated to a reversible hydrogen electrode (RHE) based on the Nernst equation of $E_{RHE} = E_{Ag/AgCl} + 0.059 * pH + 0.196$ V. Additionally, all of the obtained data were corrected against *iR* loss. All polarization curves of the obtained samples recorded after 20 cycles of cyclic voltammetry (CV) at 100 mV s^{-1} for electro-activation. Linear sweep voltammetry (LSV) curves were then recorded at a scan rate of 5 mV s^{-1} in 0.5 M H_2SO_4 condition. Chronopotentiometric (CP) and chronoamperometric (CA) tests were conducted to explore the stabilized performance of the samples in acidic media. Electrochemical impedance spectroscopy (EIS) measurements were collected under identical configuration at $\eta = 165$ mV and 150 mV for OER and HER in the frequency range from 100 kHz to 0.1 Hz, respectively. The electrochemical active surface area (ECSA) data were collected by evaluating their electrochemical double layer capacitances (C_{dl}) with CV measures. CV curves were collected in a non-Faradaic region at various scan speeds ranging from 20 to 100 mV s^{-1} at different potential range of 1.096–1.196 V vs. RHE and 0.23–0.33 V vs. RHE for OER and HER, respectively. For aicdic OWS, the same content inks of Ru/RuO_x@CN were deposited onto the surface of the tailoring 0.5×0.5 cm^2 carbon paper used as both the anode and cathode for constructing a two electrode H-type electrolyzer.

3 Results and discussion

3.1 Synthesis and morphology

Figure 1 illustrates the facile synthesis process of the Ru/RuO_x@CN sample, which involves a cascade of liquid-phase grinding followed by thermal treatment. C_3N_4 was used as the non-metallic doping precursor, which was uniformly mixed with the pristine RuO_2 to obtain a homogeneous solid powder subjected to mechanical effect and solvent evaporation process. The application of mechanical force enhances the interactions between particles, resulting in a more uniform distribution of the solid powder [46, 47]. During the subsequent controlled thermal treatment, C_3N_4 enables non-metallic doping and interfacial modulation of RuO_2, leading to the in-situ formation of a partially reduced metal Ru and RuO_2 composite heterostructure. The morphology was also displayed in Figure S1, demonstrating the well-ordered particle distribution with no evident signs of agglomeration. As shown in Figs. 2a-b, the thermal-treated Ru/RuO_x@CN sample exhibts a successful reduction in particle size, and optimized phase composition, allowing the heterostructure to be combined with the two-dimensional C_3N_4-oriented nanosheets. This resulted in a higher electrochemical active surface area, along with close and extensive contact with both the electrode and electrolyte, thereby ensuring faster interface charge transfer and higher utilization rate of the electrochemical reaction. Figure 2c displays the HRTEM image of Ru/RuO_x@CN, showing a clearly defined interface with distinct lattice fringes of 2.25 Å ascribed to the (200) lattice plane of the RuO_2 phase and 1.6 Å corresponding to the (101) lattice plane of metallic Ru, respectively, demonstrating the high-temperature generation of partially reduc ed Ru nanostructures formed onto RuO_2 substrate by design [48, 49]. Figure 2d provides an additional analysis of the SAED pattern, where several bright diffraction rings are indexed to the (110) and (200) planes of metallic Ru phase, along with the typical (101) plane of RuO_2, which are consistent with the HRTEM results [50]. Furthermore, the elemental composition of Ru/RuO_x@CN is certified by energy dispersive X-ray (EDX) elemental mapping analysis in Fig. 1e-i, which demonstrates homogeneous distributions of elements of Ru, C, O and N.

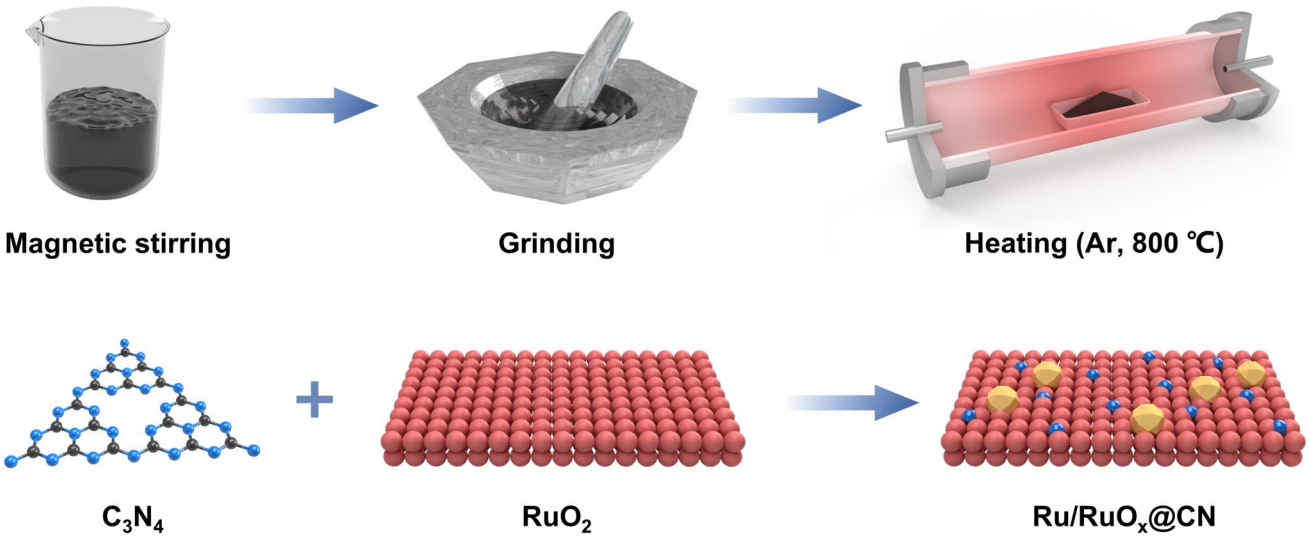

Fig. 1 Schematic illustration for the synthesis strategy of $Ru/RuO_x@CN$ catalysts

3.2 Structural characterization

The crystal structure and phase composition of the as-prepared samples were characterized by XPD pattern. As shown in Fig. 3a, all characteristic peaks of the pristine RuO_2 can align with those in the JCPDS PDF# 43–1027, while characteristic peaks corresponding to metallic Ru (JCPDS PDF#89–4903) and RuO_2 phase can be well-identified for $Ru/RuO_x@CN$, which is due to the controlled reduction of Ru species during thermal treatment [51, 52]. Furthermore, XPS analysis was conducted to investigate the electronic structure and chemical valence states of the $Ru/RuO_x@CN$ and comparative samples. Figure 3b shows the high-resolution Ru 3*p* XPS spectrum, which confirms the oxidation state of Ru species and manipulation of the interfacial chemical states through thermal treatment. The two peaks at 462.2 eV and 484.1 eV are associated with Ru $3p_{3/2}$ and Ru $3p_{1/2}$ of Ru^{4+}, which are negatively shifted in comparison with RuO_2 (464.1 eV and 486.4 eV), revealing that electrons partically transferred to Ru sites [53]. The Ru 3*d* XPS spectrum of $Ru/RuO_x@CN$ was also performed (Fig. 3c), in which the characteristic peaks at 280.4 eV and 284.5 eV can be assigned to Ru^0, peaks at 281.5 eV and 286.1 eV are related to Ru^{4+} species, respectively. Figure 3d illustrates two distinct peaks at 284.8 eV and 286.7 eV, which correspond to the C=C and C-O bonds, respectively, as deconvoluted from the C 1 *s* XPS spectrum [54]. This result suggest a notable electro-interaction between C_3N_4 and Ru/RuO_x heterostructures, indicating a potential synergy in enhancing the the overall electrochemical performance [55]. Figure 3e presents the O 1 *s* XPS spectra of the Ru/RuOx@CN sample, revealing three distinct peaks at 529.2 eV, 530.1 eV, and 531.8 eV. These peaks can be attributed to lattice oxygen species, oxygen vacancy sites and chemically adsorbed surface hydroxide (OH^-), respectively. The increase in surface oxygen vacancy sites, resulting from surface modification through controlled thermal treatment, plays a significant role in enhancing the electrochemical performance of the catalyst, facilitating the adsorption and activation of intermediates during the electrochemical processes, thereby improving reaction kinetics [56, 57]. Figure 3f displays virtually no peaks belonging to N 1 *s*, suggesting that most of nitrogen has reacted with oxygen to form a gas and has been volatilized. The above surface chemical state demonstrates that the valence of Ru decreased, revealing the formation of metallic ruthenium after co-processing with C_3N_4.

3.3 Electrocatalytic performance

The electrocatalytic performance of $Ru/RuO_x@CN$ electrocatalysts for both OER and HER was systematically investigated using a standard three-electrode configuration in an acidic electrolyte (0.5 M H_2SO_4). To investigate the effect of the chemical composition of the samples on electrochemical activities, a series of samples were prepared by adjusting the ratio of RuO_2 to C_3N_4 during synthesis, labeled as $Ru/RuO_x@CN$ 1: *x* (*x* = 2, 5, 10). Figure 4a displays the XRD patterns of the synthesized $Ru/RuO_x@CN$ samples with different precursor ratios. It can be noted that the reduction degree of Ru species increases with the increasing amount of C_3N_4. Apart from the $Ru/RuO_x@CN$ 1:2 sample, which shows a characteristic peak corresponding to the RuO_2 (100) crystal plane, the other comparison samples show only diffraction peaks attributed to metallic Ru (JCPDS PDF#89–4903). As shown in the LSV curves in Fig. 4b, the $Ru/RuO_x@CN$ 1: 2 sample requires a significantly lower

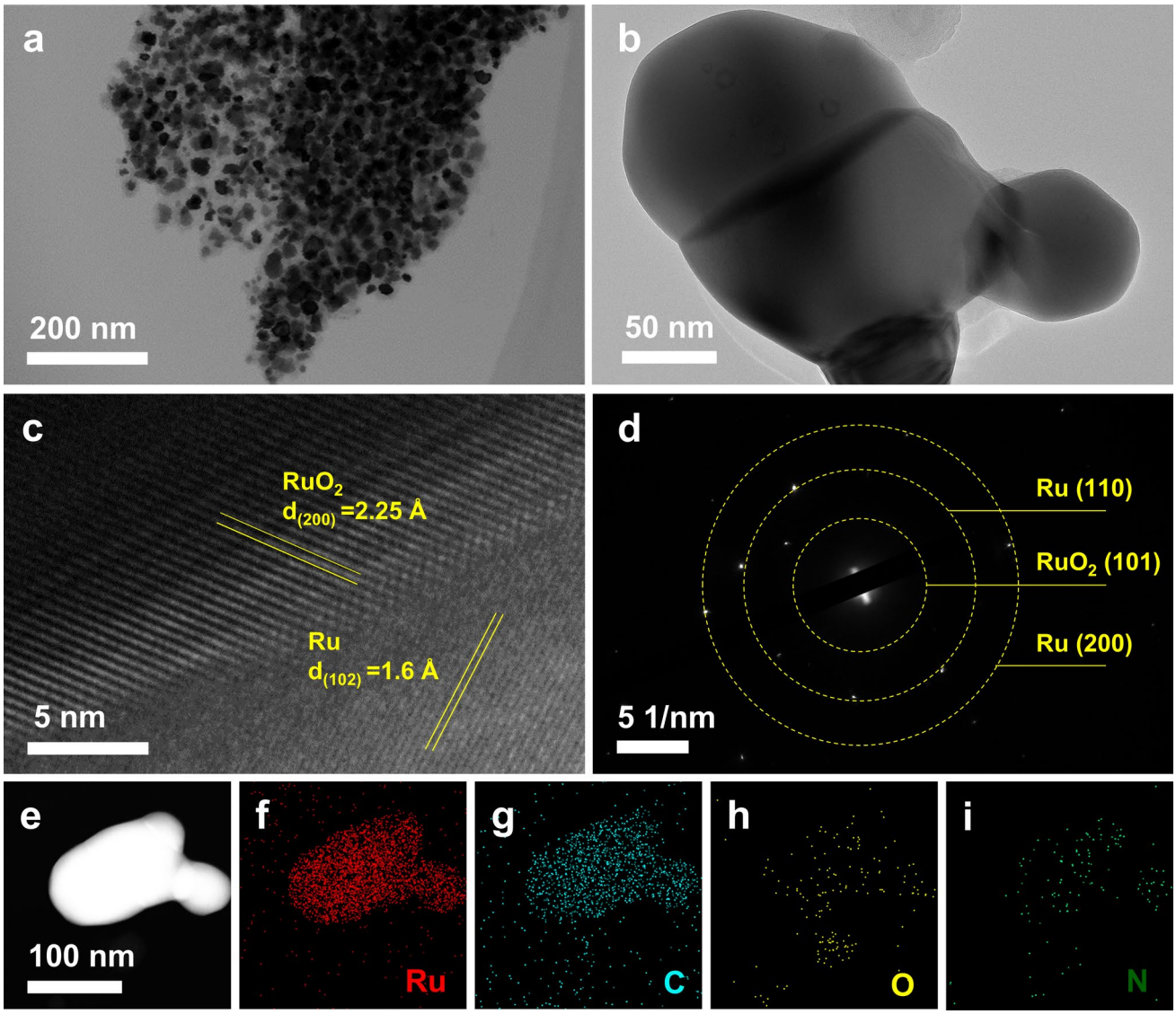

Fig. 2 Morphology characterizations of Ru/RuO_x@CN. **a**, **b** HAADF-STEM images at different magnifications, **c** HRTEM image, **d** SAED pattern, and **e**, **f**, **g**, **h**, **i** EDS elemental mapping images of Ru, C, O, and N across the typical nanostructures (scale bar: 100 nm)

overpotential to achieve a current density of 10 mA cm^{-2} for both acidic OER an d HER compared to the samples with ratios of 1: 5 and 1: 10. This indicates that the composite heterostructure of metallic Ru and RuO_2 possesses optimal electrocatalytic activity for water splitting in practical device applications, which is also consistent with the LSV curves for OER and HER processes in Figure S2. The Tafel slope curves for samples with varying precursor ratios during the acidic OER process was shown in Fig. 4c. The Ru/RuO_x@CN 1: 2 sample exhibits a relatively low Tafel slope of 62.5 mV dec^{-1}, indicating the rapid charge transfer kinetics. Based on the optimized precursor ratio, the electrocatalytic activity for acidic OER and HER of the samples prepared with different heating time was evaluated (Figure S3). As indicated in Fig. 4d, the overpotential to achieve 10 mA cm^{-2} initially increases with time and then decreases, reaching its lowest value at 2 h. Figures 4e and 4f illustrate the acidic OER and HER performance of samples synthesized at different heating temperatures. The Ru/RuO_x@CN sample synthesized at 800 °C exhibits the lowest overpotential, indicating that an appropriate heating temperature facilitates the composite structure in achieving the desired phase composition with optimized intrinsic activity.

As depicted Fig. 5a, Ru/RuO_x@CN sample demonstrates the most excellent OER catalytic performance with an overpotential of 195 mV to achieve the current density of 10 mA cm^{-2}, respectively, significantly lower than that of commercial RuO_2 (272 mV) and commercial IrO_2 (294 mV). Furthermore, Ru/RuO_x@CN exhibits a considerably decreased Tafel slope of 53.7 mV dec^{-1}, indicating a

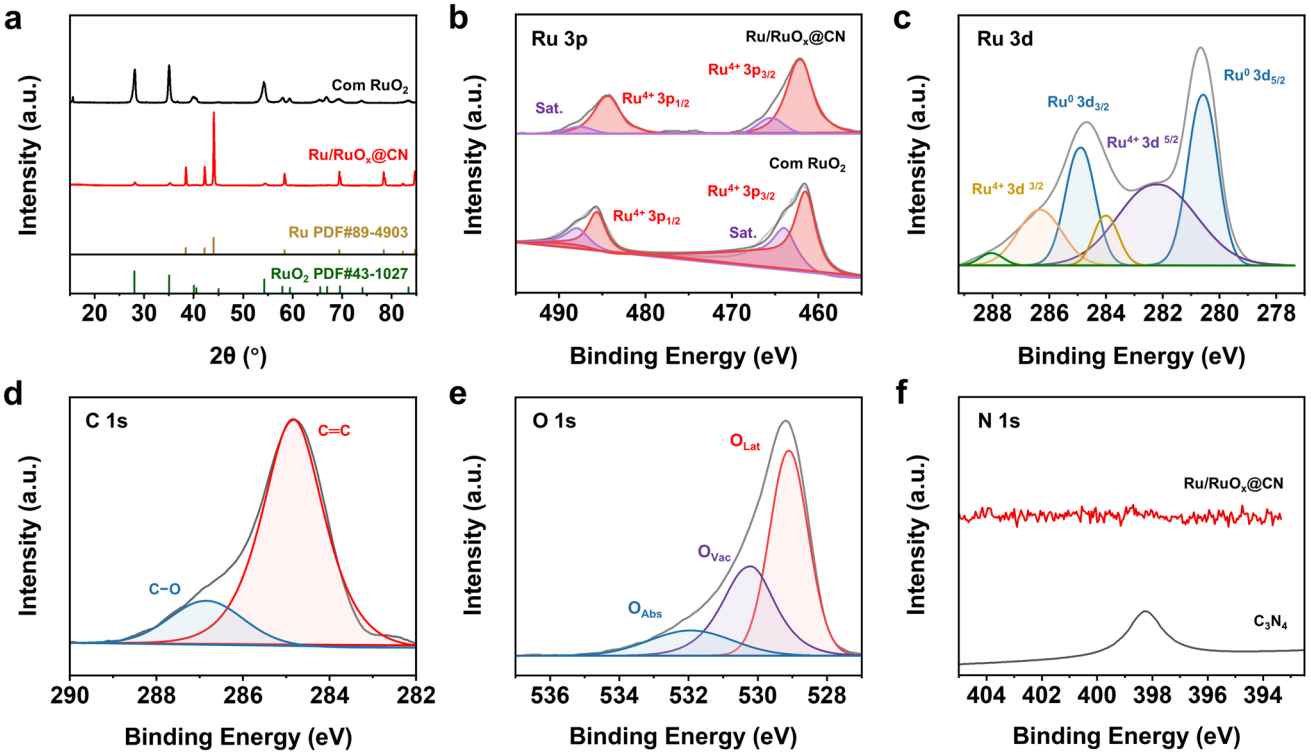

Fig. 3 Structural characterization of Ru/RuO_x@CN. **a** XRD patterns of Ru/RuO_x@CN and pristine RuO_2 samples. **b** High-resolution Ru 3*p* XPS spectra of Ru/RuO_x@CN and pristine RuO_2. **c** Ru 3*d*, **d** C 1 *s*, and **e** O 1 *s* XPS spectra of Ru/RuO_x@CN. **f** N 1 *s* XPS spectra of Ru/RuO_x@CN and C_3N_4

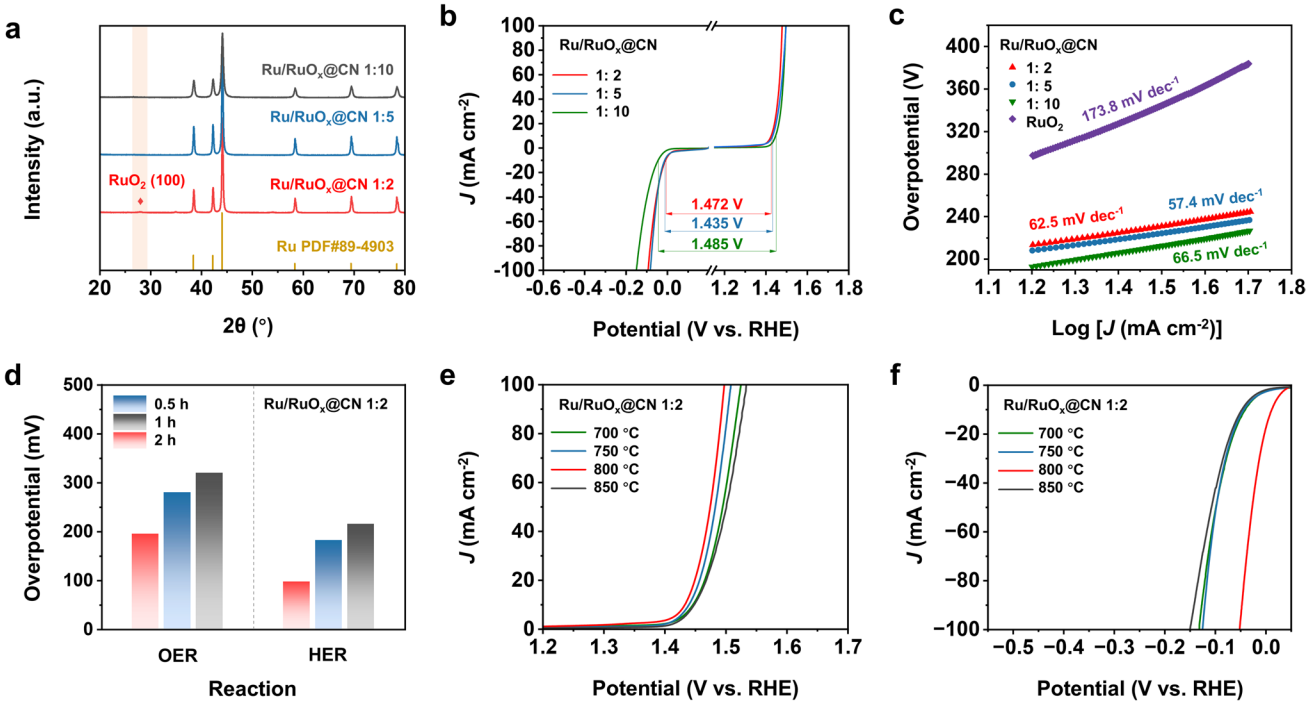

Fig. 4 Structural modulation process of Ru/RuO_x@CN catalysts. **a** XRD patterns of Ru/RuO_x@CN synthesis under various precursors ratios. **b** Electrocatalytic properties for acidic OER and HER. **c** OER Tafel Slopes of Ru/RuO_x@CN samples. **d** Overpotential values at 10 mA cm^{-2} for acidic OER and HER of Ru/RuO_x@CN 1:2 catalyst. **e**, **f** LSV curves for acidic OER and HER of Ru/RuO_x@CN synthesis at various temperatures

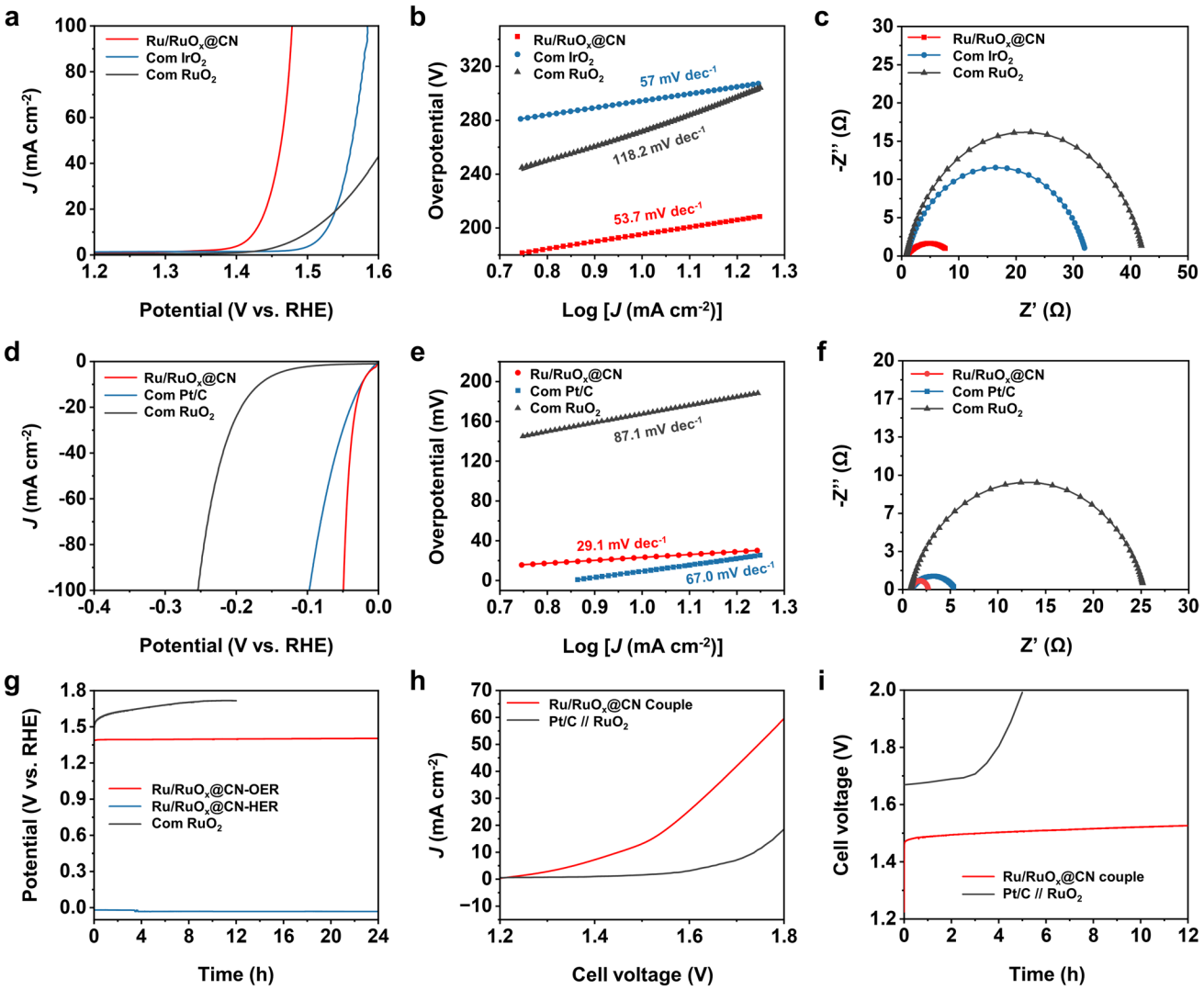

Fig. 5 Electrocatalytic properties of of Ru/RuO_x@CN and comparative catalysts. **a**, **b**, **c** LSV curves, Tafel slope plots, and Nyquist plots of Ru/RuO_x@CN, commercial IrO_2, and RuO_2 for acidic OER. **d**, **e**, **f** LSV curves, Tafel slope plots, and Nyquist plots of Ru/RuO_x@CN, commercial Pt/C, and RuO_2 for acidic HER. **g** CP curves at 10 mA cm.$^{-2}$. **h** OWS performance with a two-electrode electrolyzer. **i** CA curves of Ru/RuO_x@CN couple and Pt/C| RuO_2

much more rapid kinetic process in Ru sites after regulating the electronic structures of RuO_2 by introducing vacancies (Fig. 5b). In contrast, the fitted Tafel slopes of commercial RuO_2 and IrO_2 yield much higher values of 118.2 mV dec^{-1} and 57 mV dec^{-1}, demonstrating the sluggish OER performance. The fitted Nyquist plots in Fig. 5c and Table S1 reveal that Ru/RuO_x@CN exhibits the smallest charge transfer resistance (R_{ct}) value of 8.07 Ω compared to commercial IrO_2 (31.2 Ω) and RuO_2 (41.4 Ω), suggesting the improved charge transfer kinetics at the interface between Ru/RuO_x@CN and the electrolyte during acidic OER [58]. As illustrated in Fig. 5d, in addition to the outstanding OER performance, Ru/RuO_x@CN catalyst also demonstrates excellent activity toward HER in the acidic electrolyte. displaying an ultralow overpotential of 24.8 mV at 10 mA cm^{-2}, which is much lower than that of commercial Pt/C (26.1 mV) and RuO_2 (167 mV). Furthermore, the Ru/RuO_x@CN shows a significantly decreased Tafel slope of 29.1 mV dec^{-1} (Fig. 5e). The significant improvement in OER and HER process can be attributed to the formation of a multi-valent Ru/RuO_x heterostructure with enhanced intrinsic electrocatalytic activity. This composite facilitates rapid interfacial charge transfer, promoting the adsorption of reaction intermediates at active sites and significantly improving reaction kinetics. Additionally, the doping of the C_3N_4 substrate increases the conductivity of the catalyst, thereby reducing the interfacial impedance and ensuring more efficient surface electron transport. Moreover, faster charge transfer kinetics can be indicated by electrochemical impedance spectroscopy (EIS) from the Nyquist plots in Fig. 5f, where the Ru/

RuO_x@CN also exhibits the smallest R_{ct} value of 1.73 Ω among various samples (Table S2). Long-term durability measurement is also critical for evaluating the electrocatalytic performance. To assess the electrochemically active surface area (ECSA), the double-layer capacitances (C_{dl}) of samples were calculated in Figure S4 using a standard cyclic voltammetry (CV) scan in the non-Faradaic region, with scan rates from 20 to 100 mV s^{-1} [59]. The CV curves for acidic OER and HER processes were shown in Figures S5 and S6, respectivelty. The Ru/RuO_x@CN catalyst exhibited the highest C_{dl} value of 122.7 and 154.6 mF cm^{-2} compared to commercial IrO_2, Pt/C and RuO_2 samples, indicating the highest ESCA value and more exposure of catalytic active sites. The OER and HER stability of Ru/RuO_x@CN sampel was tested by CP measurement. As displayed in Fig. 5g, Ru/RuO_x@CN demonstrates the most excellent stability with negligible change after continuous operation for both OER and HER processes after 24 h, in contrast to the commercial RuO_2, which shows significant potential changes in less than 4 h. The evaluation of electrochemical durability demonstrates the significant contribution of oxygen vacancies in Ru/RuO_x@CN to prevent Ru sites from overoxidation and enhance durable OER ability in acidic media. In addition, the post-reaction morphology of Ru/RuO_x@CN was characterized by TEM images in Figure S7, where the composite heterostructure consisting of metallic Ru and RuO_2 is still observable. This demonstrates the catalyst's excellent structural stability after long-term operation. Benefiting from the excellent OER and HER performance, a two-electrode proton exchange membrane (PEM) configuration was constructed using bifunctional Ru/RuO_x@CN as both the cathode and anode. An electrolyzer based on commercial Pt/C coupled with commercial RuO_2 was also fabricated for comparation. As depicted in Fig. 5h, Ru/RuO_x@CN couple demonstrates outstanding activity with a cell voltage of only 1.53 V to achieve 10 mA cm^{-2}, which is lower than that of Pt/C || RuO_2 (1.58 V). Additionally, the long-term stability of Ru/RuO_x@CN couple for OWS was evaluated through CA test at 10 mA cm^{-2} (Fig. 5i). Over a continuous 12-h test, the cell voltage shows negligible degradation. The excellent electrochemical durability of Ru/RuO_x@CN provides an important guarantee for practical application in PEM electrolyzers.

4 Conclusion

In conclusion, a composite Ru/RuOx@CN electrocatalyst was successfully synthesised by a facile cascading method involving grinding with C_3N_4 followed by thermal treatment. This catalyst exhibits remarkable electrocatalytic activity, achieving ultralow overpotentials of 197 mV for the OER and 24.8 mV for HER at a current density of 10 mA cm^{-2} in acidic media. Furthermore, Ru/RuOx@CN effectively serves as a bifunctional electrocatalyst in an acid-based electrolyzer, driving a current density of 10 mA cm^{-2} with a low applied cell voltage of only 1.53 V. The outstanding performance of Ru/RuOx@CN can be mainly attributed to the efficient charge transfer and increased exposure of active sites. This study highlights the potential of Ru/RuOx@CN as a promising alternative to high-cost noble metal catalysts and provides valuable insights for the development of efficient and stable Ru-based electrocatalysts for sustainable hydrogen production.

Supplementary Information The online version contains supplementary material available at https://doi.org/10.1007/s42114-025-01234-z.

Author contribution X. X. and Y. Z. contributed equally to this work. P. D., R. W. and K. H. conceived the idea and designed the research. X. X. and Y. Z prepared the materials and fabricated the electrocatalysts. X. X., Y. Z. and M. L. performed the micromorphology experiments and analysis. Y. Z. and Y. Q. performed the structural characterizations and analysis. X. X and J. W. performed the electrocatalytic experiments and analysis. All the authors contributed to the writing of the paper.

Funding This study is supported by the National Natural Science Foundations of China (Grant Nos. 61874013 and 61874014), Fundamental Research Funds for the Central Universities (2023ZCJH03), Beijing Municipal Science& Technology Commission, Administrative Commission of Zhongguancun Science Park No. Z231100006023020, Fund of State Key Laboratory of Information Photonics and Optical Communications (Beijing University of Posts and Telecommunications, P.R. China), and Teaching Reform Projects at BUPT (2022CXCY-B03).

Data availability No datasets were generated or analysed during the current study.

Declarations

Competing interests The authors declare no competing interests.

Open Access This article is licensed under a Creative Commons Attribution-NonCommercial-NoDerivatives 4.0 International License, which permits any non-commercial use, sharing, distribution and reproduction in any medium or format, as long as you give appropriate credit to the original author(s) and the source, provide a link to the Creative Commons licence, and indicate if you modified the licensed material. You do not have permission under this licence to share adapted material derived from this article or parts of it. The images or other third party material in this article are included in the article's Creative Commons licence, unless indicated otherwise in a credit line to the material. If material is not included in the article's Creative Commons licence and your intended use is not permitted by statutory regulation or exceeds the permitted use, you will need to obtain permission directly from the copyright holder. To view a copy of this licence, visit http://creativecommons.org/licenses/by-nc-nd/4.0/.

References

1. Seh ZW, Kibsgaard J, Dickens CF, Chorkendorff I, Nørskov JK, Jaramillo TF (2017) Combining theory and experiment

in electrocatalysis: insights into materials design. Science 355(6321):eaad4998. https://doi.org/10.1126/science.aad4998
2. Boettcher SW, Surendranath Y (2021) Heterogeneous electrocatalysis goes chemical. Nature. Catalysis 4(1):4–5. https://doi.org/10.1038/s41929-020-00570-1
3. Gautam J, Lee S-Y, Park S-J (2024) Copper-doped zinc cobalt sulfide nanosheets as advanced bifunctional electrocatalysts for sustainable hydrogen production via electrochemical water splitting. Adv Compos Hybrid Mater 7(5):155. https://doi.org/10.1007/s42114-024-00985-5
4. Liu R-T, Xu Z-L, Li F-M, Chen F-Y, Yu J-Y, Yan Y, Chen Y, Xia BY (2023) Recent advances in proton exchange membrane water electrolysis. Chem Soc Rev 52(16):5652–5683. https://doi.org/10.1039/d2cs00681b
5. Li G, Shen R, Hu S, Wang B, Algadi H, Wang C (2022) Norbornene-based acid–base blended polymer membranes with low ion exchange capacity for proton exchange membrane fuel cell. Adv Compos Hybrid Mater 5(3):2131–2137. https://doi.org/10.1007/s42114-022-00559-3
6. Lin X, Chen L, Zhong X, BaQais A, Dang W, Amin MA, Huang H, Li H, Liang G, Liu G, Yang Z (2023) N-doped bimetallic phosphides composite catalysts derived from metal–organic frameworks for electrocatalytic water splitting. Adv Compos Hybrid Mater 6(2):79. https://doi.org/10.1007/s42114-023-00660-1
7. Zhao J, Bao K, Xie M, Wei D, Yang K, Zhang X, Zhang C, Wang Z, Yang X (2022) Two-dimensional ultrathin networked CoP derived from $Co(OH)_2$ as efficient electrocatalyst for hydrogen evolution. Adv Compos Hybrid Mater 5(3):2421–2428. https://doi.org/10.1007/s42114-022-00455-w
8. Wang H, Qi H, Sun X, Jia S, Li X, Miao TJ, Xiong L, Wang S, Zhang X, Liu X, Wang A, Zhang T, Huang W, Tang J (2023) High quantum efficiency of hydrogen production from methanol aqueous solution with PtCu–TiO_2 photocatalysts. Nat Mater 22(5):619–626. https://doi.org/10.1038/s41563-023-01519-y
9. Rong C, Dastafkan K, Wang Y, Zhao C (2023) Breaking the activity and stability bottlenecks of electrocatalysts for oxygen evolution reactions in acids. Adv Mater 35(49):2211884. https://doi.org/10.1002/adma.202211884
10. Wang Q, Cheng Y, Tao H B, Liu Y, Ma X, Li D S, Yang H B, Liu B (2023) Long-term stability challenges and opportunities in acidic oxygen evolution electrocatalysis. Angewandte Chemie International Edition 62(11). https://doi.org/10.1002/anie.202216645
11. Aitbekova A, Zhou C, Stone ML, Lezama-Pacheco JS, Yang A-C, Hoffman AS, Goodman ED, Huber P, Stebbins JF, Bustillo KC, Ercius P, Ciston J, Bare SR, Plessow PN, Cargnello M (2022) Templated encapsulation of platinum-based catalysts promotes high-temperature stability to 1,100 °C. Nat Mater 21(11):1290–1297. https://doi.org/10.1038/s41563-022-01376-1
12. Wei J, Tang H, Sheng L, Wang R, Fan M, Wan J, Wu Y, Zhang Z, Zhou S, Zeng J (2024) Site-specific metal-support interaction to switch the activity of Ir single atoms for oxygen evolution reaction. Nat Commun 15(1):559. https://doi.org/10.1038/s41467-024-44815-0
13. Pan X, Du W, Zhao X, Chang G, Zhao Z, Li C, Lei M (2022) Efficient exfoliation method of sodium-ruthenium composites for acid water oxidation. Adv Compos Hybrid Mater 5(3):2536–2545. https://doi.org/10.1007/s42114-022-00521-3
14. Huang K, Lin C, Yu G, Du P, Xie X, He X, Zheng Z, Sun N, Tang H, Li X, Lei M, Wu H (2022) Ru/Se-RuO_2 composites via controlled selenization strategy for enhanced acidic oxygen evolution. Adv Funct Mater 33(8). https://doi.org/10.1002/adfm.202211102
15. Ge R, Chen L (2022) Ultra-small RuO2 nanoparticles supported on carbon cloth as a high-performance pseudocapacitive electrode. Adv Compos Hybrid Mater 5(2):696–703. https://doi.org/10.1007/s42114-022-00452-z
16. Du P, Lin C, He X, Zheng Z, Xie X, Huang K, Lei M, Tang H (2023) Controlled fabrication of Ru–O–Se composites for enhanced acidic oxygen evolution. Adv Compos Hybrid Mater 6(1):40. https://doi.org/10.1007/s42114-023-00624-5
17. Wang J, Cheng C, Yuan Q, Yang H, Meng F, Zhang Q, Gu L, Cao J, Li L, Haw S-C, Shao Q, Zhang L, Cheng T, Jiao F, Huang X (2022) Exceptionally active and stable RuO_2 with interstitial carbon for water oxidation in acid. Chem. https://doi.org/10.1016/j.chempr.2022.02.003
18. Wang K, Wang Y, Yang B, Li Z, Qin X, Zhang Q, Lei L, Qiu M, Wu G, Hou Y (2022) Highly active ruthenium sites stabilized by modulating electron-feeding for sustainable acidic oxygen-evolution electrocatalysis. Energy Environ Sci. https://doi.org/10.1039/D1EE03610F
19. Hao S, Liu M, Pan J, Liu X, Tan X, Xu N, He Y, Lei L, Zhang X (2020) Dopants fixation of Ruthenium for boosting acidic oxygen evolution stability and activity. Nat Commun 11(1):5368. https://doi.org/10.1038/s41467-020-19212-y
20. Wu ZY, Chen FY, Li B, Yu SW, Finfrock YZ, Meira DM, Yan QQ, Zhu P, Chen MX, Song TW, Yin Z, Liang HW, Zhang S, Wang G, Wang H (2022) Non-iridium-based electrocatalyst for durable acidic oxygen evolution reaction in proton exchange membrane water electrolysis. Nat Mater. https://doi.org/10.1038/s41563-022-01380-5
21. Dang Y, Wu T, Tan H, Wang J, Cui C, Kerns P, Zhao W, Posada L, Wen L, Suib SL (2021) Partially reduced Ru/RuO_2 composites as efficient and pH-universal electrocatalysts for hydrogen evolution. Energy Environ Sci 14(10):5433–5443. https://doi.org/10.1039/d1ee02380b
22 Zhang L, Jang H, Liu H, Kim MG, Yang D, Liu S, Liu X, Cho J (2021) Sodium-decorated amorphous/crystalline RuO_2 with rich oxygen vacancies: a robust pH-universal oxygen evolution electrocatalyst. Angewandte Chemie International Edition 60(34):18821–18829. https://doi.org/10.1002/anie.202106631
23. Wang X, Wan X, Qin X, Chen C, Qian X, Guo Y, Xu Q, Cai W-B, Yang H, Jiang K (2022) Electronic structure modulation of RuO_2 by TiO_2 enriched with oxygen vacancies to boost acidic O2 evolution. ACS Catal 12(15):9437–9445. https://doi.org/10.1021/acscatal.2c01944
24. Wang Y, Yang R, Ding Y, Zhang B, Li H, Bai B, Li M, Cui Y, Xiao J, Wu Z-S (2023) Unraveling oxygen vacancy site mechanism of Rh-doped RuO_2 catalyst for long-lasting acidic water oxidation. Nat Commun 14(1):1412. https://doi.org/10.1038/s41467-023-37008-8
25. Zhao Z, Lin Y, Wu J, Li J, Lei M (2022) Mixed-phase cobalt-based nanosheets prepared by rapid thermal annealing for oxygen evolution catalysis. Adv Compos Hybrid Mater 5(3):2589–2600. https://doi.org/10.1007/s42114-022-00537-9
26. Yin J, Jin J, Lu M, Huang B, Zhang H, Peng Y, Xi P, Yan CH (2020) Iridium single atoms coupling with oxygen vacancies boosts oxygen evolution reaction in acid media. J Am Chem Soc 142(43):18378–18386. https://doi.org/10.1021/jacs.0c05050
27. Chen K, Cao Y-H, Kim G-C, Kim C, Yadav S, Dao V, Lee I-H (2024) Synergism of electronic modulation and geometric architecture: bimetallic phosphide heterostructure on nickel foam for efficient water splitting. Adv Compos Hybrid Mater 7(2):71. https://doi.org/10.1007/s42114-024-00875-w
28. Hao Y-R, Xue H, Lv L, Sun J, Guo N, Song T, Dong H, Zhang J, Wang Q (2021) Unraveling the synergistic effect of defects and interfacial electronic structure modulation of pealike CoFe@Fe_3N to achieve superior oxygen reduction performance. Appl Catal B: Environ 295:120314. https://doi.org/10.1016/j.apcatb.2021.120314
29. Adegbesan C D, Daniel S, Monguen C K F, Otieno H N, Tian Z-Y (2024) Catalytically active Cu-Fe/kaolin hybrid catalyst

for semi-hydrogenation of acetylene. Eng Sci. https://doi.org/10.30919/es1148
30. Natarajan V K, Madswamy S L, Krishnamoorthy N, Ramamoorthy G, Dhanusuraman R (2023) Ultrasonication-assisted synthesis of nickel tungstate decorated on polydimethoxyaniline nanocomposite catalyst for potential direct methanol fuel cell application. ES Energy Environ. https://doi.org/10.30919/esee926
31. AbdulRasheed T, Afotey B, Ankudey E G, Anang D A (2023) Synthesis and characterization of novel calcium oxide/calcium ferrite, $CaO/CaFe_2O_4$ composite nanocatalyst for biodiesel production. ES Mater Manuf. https://doi.org/10.30919/esmm922
32. Vengadesan K, Madaswamy SL, Natarajan VK, Siddiqui MR, Wabaidur SM, Eswaran M, Dhanusuraman R (2023) Electrochemical fabrication of nano-structured poly(dimethoxyaniline)-platinum hybrid materials: an efficient anode electrocatalyst for oxidation of methanol. ES Energ Environ. https://doi.org/10.30919/esee8c858
33. Salunke JY, Yadav GD (2023) Lanthanum doped zirconia as an efficient catalyst for reductive amination of 2-methoxybenzaldehyde with dimethylformamide via Leuckart type reaction. ES Mater Manuf. https://doi.org/10.30919/esmm5f853
34 Marschall R, Wang L (2014) Non-metal doping of transition metal oxides for visible-light photocatalysis. Catal Today 225:111–135. https://doi.org/10.1016/j.cattod.2013.10.088
35. Guo H, Yang C-Y, Zhang X, Motta A, Feng K, Xia Y, Shi Y, Wu Z, Yang K, Chen J, Liao Q, Tang Y, Sun H, Woo HY, Fabiano S, Facchetti A, Guo X (2021) Transition metal-catalysed molecular n-doping of organic semiconductors. Nature 599(7883):67–73. https://doi.org/10.1038/s41586-021-03942-0
36. Chen C-Y, Tseng C-C (2022) Two-dimensional Ga_2S_3/g-C_3N_4 heterojunction composites with highly enhanced photocatalytic activity and stability. Adv Compos Hybrid Mater 6(1):20. https://doi.org/10.1007/s42114-022-00606-z
37 Shi Z, Yang W, Gu Y, Liao T, Sun Z (2020) Metal-nitrogen-doped carbon materials as highly efficient catalysts: progress and rational design. Adv Sci 7(15):2001069. https://doi.org/10.1002/advs.202001069
38. Wang H, Thangamuthu M, Wu Z, Yang J, Yuan H, Bayazit MK, Tang J (2022) Self-assembled sulphur doped carbon nitride for photocatalytic water reforming of methanol. Chem Eng J 445:136790. https://doi.org/10.1016/j.cej.2022.136790
39. Ishida T, Kinoshita N, Okatsu H, Akita T, Takei T, Haruta M (2008) Influence of the support and the size of gold clusters on catalytic activity for glucose oxidation. Angew Chem Int Ed Engl 47(48):9265–9268. https://doi.org/10.1002/anie.200802845
40. Ji M, Yang X, Chang S, Chen W, Wang J, He D, Hu Y, Deng Q, Sun Y, Li B, Xi J, Yamada T, Zhang J, Xiao H, Zhu C, Li J, Li Y (2021) RuO_2 clusters derived from bulk $SrRuO_3$: robust catalyst for oxygen evolution reaction in acid. Nano Res. https://doi.org/10.1007/s12274-021-3843-8
41. Zagalskaya A, Alexandrov V (2020) Role of defects in the interplay between adsorbate evolving and lattice oxygen mechanisms of the oxygen evolution reaction in RuO_2 and IrO_2. ACS Catal 10(6):3650–3657. https://doi.org/10.1021/acscatal.9b05544
42. Xia C, Wang H, Kim JK, Wang J (2021) Rational design of metal oxide-based heterostructure for efficient photocatalytic and photoelectrochemical systems. Adv Funct Mater 31(12):2008247. https://doi.org/10.1002/adfm.202008247
43. Lu Q, Wu H, Zheng X, Cao Y, Li J, Wang Y, Wang H, Zhi C, Deng Y, Han X, Hu W (2022) Controllable constructing janus homologous heterostructures of transition metal alloys/sulfides for efficient oxygen electrocatalysis. Adv Energy Mater 12(42):2202215. https://doi.org/10.1002/aenm.202202215
44. Deng Z, Zhang Q, Deng Q, Guo Z, Seok I (2021) Modification of coconut shell activated carbon and purification of volatile organic waste gas acetone. Adv Compos Hybrid Mater. https://doi.org/10.1007/s42114-021-00345-7
45. Bag PP (2021) Externally mechanical force induced unusual defect in the second polymorph of isoniazid/fumaric acid co-crystal. Eng Sci. https://doi.org/10.30919/es8d1004
46. Robertson JC, Coote ML, Bissember AC (2019) Synthetic applications of light, electricity, mechanical force and flow. Nat Rev Chem 3(5):290–304. https://doi.org/10.1038/s41570-019-0094-2
47. Hu Y, Li B, Yu C, Fang H, Li Z (2023) Mechanochemical preparation of single atom catalysts for versatile catalytic applications: a perspective review. Mater Today. https://doi.org/10.1016/j.mattod.2023.01.019
48. Lin C, Li J-L, Li X, Yang S, Luo W, Zhang Y, Kim S-H, Kim D-H, Shinde SS, Li Y-F, Liu Z-P, Jiang Z, Lee J-H (2021) In-situ reconstructed Ru atom array on α-MnO_2 with enhanced performance for acidic water oxidation. Nat Catal 4(12):1012–1023. https://doi.org/10.1038/s41929-021-00703-0
49. Cui X, Ren P, Ma C, Zhao J, Chen R, Chen S, Rajan NP, Li H, Yu L, Tian Z, Deng D (2020) Robust interface Ru centers for high-performance acidic oxygen evolution. Adv Mater 32(25):e1908126. https://doi.org/10.1002/adma.201908126
50. Zhou C, Zhao S, Meng H, Han Y, Jiang Q, Wang B, Shi X, Zhang W, Zhang L, Zhang R (2021) $RuCoO_x$ Nanofoam as a high-performance trifunctional electrocatalyst for rechargeable zinc-air batteries and water splitting. Nano Lett 21(22):9633–9641. https://doi.org/10.1021/acs.nanolett.1c03407
51. Qin R, Wang P, Li Z, Zhu J, Cao F, Xu H, Ma Q, Zhang J, Yu J, Mu S (2021) Ru-incorporated nickel diselenide nanosheet arrays with accelerated adsorption kinetics toward overall water splitting. Small 18(6). https://doi.org/10.1002/smll.202105305
52. Huang H, Kim H, Lee A, Kim S, Lim W-G, Park C-Y, Kim S, Kim S-K, Lee J (2021) Structure engineering defective and mass transfer-enhanced RuO_2 nanosheets for proton exchange membrane water electrolyzer. Nano Energy 88. https://doi.org/10.1016/j.nanoen.2021.106276
53. Wang C, Qi L (2020) Heterostructured inter-doped ruthenium-cobalt oxide hollow nanosheet arrays for highly efficient overall water splitting. Angew Chem Int Ed Engl 59(39):17219–17224. https://doi.org/10.1002/anie.202005436
54. Xing Y, Wang K, Li N, Su D, Wong W-T, Huang B, Guo S (2020) Ultrathin RuRh alloy nanosheets enable high-performance lithium-CO_2 battery. Matter 2(6):1494–1508. https://doi.org/10.1016/j.matt.2020.02.020
55. Wang J, Ji Y, Yin R, Li Y, Shao Q, Huang X (2019) Transition metal-doped ultrathin RuO_2 networked nanowires for efficient overall water splitting across a broad pH range. J Mater Chem A 7(11):6411–6416. https://doi.org/10.1039/c9ta00598f
56. Miao X, Zhang L, Wu L, Hu Z, Shi L, Zhou S (2019) Quadruple perovskite ruthenate as a highly efficient catalyst for acidic water oxidation. Nat Commun 10(1):3809. https://doi.org/10.1038/s41467-019-11789-3
57. Qiu Y, Rao Y, Zheng Y, Hu H, Zhang W, Guo X (2022) Activating ruthenium dioxide via compressive strain achieving efficient multifunctional electrocatalysis for Zn-air batteries and overall water splitting. InfoMat. https://doi.org/10.1002/inf2.12326
58. Chen D, Liu T, Wang P, Zhao J, Zhang C, Cheng R, Li W, Ji P, Pu Z, Mu S (2020) Ionothermal route to phase-Pure RuB_2 catalysts for efficient oxygen evolution and water splitting in acidic media. ACS Energy Lett 5(9):2909–2915. https://doi.org/10.1021/acsenergylett.0c01384
59. Liu G, Zhou W, Chen B, Zhang Q, Cui X, Li B, Lai Z, Chen Y, Zhang Z, Gu L, Zhang H (2019) Synthesis of RuNi alloy nanostructures composed of multilayered nanosheets for highly efficient electrocatalytic hydrogen evolution. Nano Energy 66. https://doi.org/10.1016/j.nanoen.2019.104173

Publisher's Note Springer Nature remains neutral with regard to jurisdictional claims in published maps and institutional affiliations.